A Type II n-n Staggered Orthorhombic V_2O_5/ Monoclinic Clinobisvanite $BiVO_4$ Heterojunction Photoanode for Photoelectrochemical Water Oxidation: Fabrication, Characterisation and Experimental Validation

Chong Siang Yaw[1], Qiushi Ruan[2], Junwang Tang[2], Ai Kah Soh[3], Meng Nan Chong[1,4*]

[1] School of Engineering, Chemical Engineering Discipline, Monash University Malaysia, Jalan Lagoon Selatan, Bandar Sunway, Selangor Darul Ehsan 47500, Malaysia

[2] Department of Chemical Engineering, University College London, Torrington Place, London WC1E 7JE, United Kingdom

[3] School of Engineering, Mechanical Engineering Discipline, Monash University Malaysia, Jalan Lagoon Selatan, Bandar Sunway, Selangor Darul Ehsan 47500, Malaysia

[4] Sustainable Water Alliance, Advanced Engineering Platform, Monash University Malaysia, Jalan Lagoon Selatan, Bandar Sunway, Selangor DE 47500, Malaysia

[*]Corresponding author:

Associate Professor Dr. Meng Nan Chong

School of Engineering, Chemical Engineering Discipline, Monash University Malaysia, Jalan Lagoon Selatan, Bandar Sunway, Selangor DE 47500 Malaysia

Email: Chong.Meng.Nan@monash.edu

Abstract

Conventional photoanode using a singular semiconductor material is not technically viable for photoelectrochemical (PEC) water oxidation owing to the properties relating to its wide band gap, sluggish charge mobility, as well as poor separation and rapid recombination of photogenerated charge carriers. The main aim of this study was to fabricate an *n*-*n* heterojunction photoanode of V_2O_5/$BiVO_4$ via a facile electrodeposition synthesis method in order to overcome the technical bottlenecks encountered in conventional singular photoanode structures. Additionally, the synergistic effect of band potentials matching and conductivity difference between $BiVO_4$ and V_2O_5 were studied using LSV, IMPS, EIS, HR-TEM, XRD, XPS, Raman and ultraviolet-visible spectroscopies. This was followed by the performance evaluation of the light-induced water splitting using a standard three-electrode assembly PEC cell under 1.5 AM solar simulator. Results showed that the V_2O_5/$BiVO_4$ heterojunction photoanode achieved a significantly improved photocurrent density of 1.53 mA/cm^2 at 1.5 V vs Ag/AgCl, which was a 6.9-fold and a 7.3-fold improvement over the individual pristine $BiVO_4$ (0.22 mA/cm^2) and V_2O_5 (0.21 mA/cm^2), respectively. The improvement was attributed to the lower charge resistances at the FTO/semiconductor, semiconductor/FTO and semiconductor/electrolyte interfaces as well as the fast transit time (τ) of 6.4 millisecond for photo-injected electrons in the V_2O_5/$BiVO_4$ heterojunction photoanode. Finally, the experimental results were used to reconstruct a theoretical band diagram in validating the heterojunction alignment between V_2O_5 and $BiVO_4$ as well as in elucidating the photogenerated charge carriers transfer mechanism in the V_2O_5/$BiVO_4$ heterojunction photoanode.

Key words: Bismuth vanadate; *n*-*n* heterojunction; Photoelectrocatalysis; Charge separation

1. Introduction

Photoelectrochemical (PEC) water splitting, also known as artificial photosynthesis, is a green route for sustainable hydrogen (H_2) production by harnessing the largest abundant renewable solar energy and convert them into chemical fuels [1]. However, the PEC-based technology for water splitting has yet to be commercialised due to the high H_2 production cost and significant efficiency losses with oxygen (O_2) production [2]. In this instance, the identification of a suitable semiconductor-based photoelectrode for PEC water splitting plays an important role in reducing the costs of materials and processes as well as improving the H_2 yield [3]. There are a few important considerations that must be taken into account when considering the type of semiconductor photoelectrode used, such as: (1) appropriate alignment of conduction (CB) and valance band (VB) edge positions for H_2 and O_2 generations, respectively, (2) being a good light absorber by possessing a reasonably narrow band gap that could be activated under the visible light spectrum, and (3) stable against most of the chemical and photochemical externalities [4].

To date, various type of semiconductor photoelectrodes (e.g. TiO_2, Fe_2O_3, WO_3 and $BiVO_4$) have garnered significant interests and exploitation for PEC water splitting after the pioneering work by Fujishima and Honda in 1972 [5]. Among the suitable candidate of semiconductor photoelectrodes, ternary metal oxides monoclinic $BiVO_4$ is one of the most promising photoanode candidates used for PEC water splitting under visible light [6]. Theoretically, $BiVO_4$ is able to absorb a substantial portion of visible range spectrum due to it is having a direct band gap of 2.5 eV. Additionally, $BiVO_4$ also has a favourable CB edge position near 0 V_{RHE} and exhibits high resistance towards photoinduced corrosion near neutral aqueous condition due to its oxygen evolution reaction (OER), which is slightly more positive than the

water oxidation potential [7]. Based on its band gap energy, the theoretical maximum solar-to-hydrogen (STH) efficiency for $BiVO_4$ is approximately 9.1%, while the theoretical maximum photocurrent density is approximately 6.47 mA/cm^2 at 1.23 V_{RHE} under 1 Sun illumination [8].

Despite the multi-merits of $BiVO_4$ used as a photoanode in PEC water oxidation, the practical potential is still far reaching from its full potential in terms of the photocurrent generation [9]. This is due to that $BiVO_4$ is suffering from its inherent material drawbacks, such as poor separation of photogenerated charge carriers and high bulk and surface recombination, which predominantly cause by the sluggish charge mobility of the electron-hole pairs [10]. In this aspect, the mobility of the photogenerated electrons is limited by the distance between the VO_4 tetrahedra of pristine $BiVO_4$ crystal (i.e. V-3d orbitals where the CB lie), while the transfer of photogenerated holes across the semiconductor-electrolyte interface depends on the kinetics of four-electron water oxidation reaction [10]. Thus, the most commonly reported photocurrent generation values in the literature for using pristine $BiVO_4$ as the photoanode in PEC water oxidation are approximately 0.5 mA/cm^2 [11].

Various surface and interfacial modifications have been made thus far to improve the PEC performance of pristine $BiVO_4$, such as the introduction of metal dopants as active recombination centers [12-15], coupling of $BiVO_4$ with OER catalyst to improve the mobility of photogenerated charge carriers during water oxidation reaction [16-19], and the incorporation of $BiVO_4$ with other semiconductors to form heterojunction photoelectrode to promote effective transfer of photogenerated charge carriers [16, 20-23]. As of recent, the fabrication of heterojunction photoelectrode by creating a region with electric potential gradients between the interfaces of two semiconductors is proven to be an effective approach for good separation and transfer rate of photogenerated charge carriers [24]. Typically, there are three type of

heterojunction alignments between two semiconductors and they are Type I: Straddling gap, Type II: Staggered gap and Type III: Broken gap, depending on their band gap properties and alignment of CB and VB edges. Cheng et al. discussed that the Type II heterojunction alignment is the most potent structure to overcome the poor separation of photogenerated charge carriers in semiconductors [25].

Previous studies have attempted the fabrication of heterojunction photoanodes of $BiVO_4$ with WO_3 [26, 27], ZnO [28, 29] and TiO_2 [25, 30]. However, the photocurrent generation was ranging from 0.8 – 6.72 mA/cm^2 at 1.23 V vs RHE where the heterojunction photoanodes with the highest photocurrent reported to date is CoPi-coated WO_3/$BiVO_4$ with 6.72 mA/cm^2 at 1.23 V vs RHE [27]. From the literature, it was evidenced that there are no previous work that considered on forming heterojunction photoanode between $BiVO_4$ and vanadium pentoxide (V_2O_5) for PEC water oxidation. V_2O_5 is an infrequently studied *n*-type semiconductor for PEC water splitting with a band gap energy of 2.3 eV, which is smaller than that of $BiVO_4$. This enables V_2O_5 to absorb visible light more efficiently, and its band edge potentials are able to straddle the redox potential of water at 1.23 eV [31]. The formation of heterojunction photoanodes between V_2O_5 and other semiconductors, such as TiO_2 [32], ZnO [33] and g-C_3N_4 [34] is able to promote the photocatalytic efficiency by extending the range of light absorption as well as improving the charge mobility and the good separation of photogenerated charge carriers.

This study aimed to fabricate an *n*-*n* heterojunction photoanode of V_2O_5/$BiVO_4$ via a facile electrodeposition synthesis method over the transparent and conductive fluorine-doped tin oxide (FTO) substrate. The synergistic effect of band potentials matching and conductivity difference between $BiVO_4$ and V_2O_5 were studied using linear sweep voltammetry (LSV), intensity modulated photocurrent spectroscopy (IMPS), electrochemical impedance spectroscopy (EIS),

high resolution-transmission electron microscopy (HR-TEM), X-ray diffractometer (XRD), X-ray photoelectron spectroscopy (XPS), Raman spectroscopy and ultraviolet-visible (UV-vis) spectroscopy. This was followed by the performance evaluation of the light-induced water splitting using a standard three-electrode assembly PEC cell under 1.5 AM solar simulator. Finally, the experimental results were used to reconstruct a theoretical band diagram in validating the heterojunction alignment between V_2O_5 and $BiVO_4$ as well as in elucidating the photogenerated charge carriers transfer mechanism in the $V_2O_5/BiVO_4$ heterojunction photoanode.

2. Experimental Section

2.1. Materials

Bismuth nitrate pentahydrate ($Bi(NO_3)_3.5H_2O$) was purchased from R&M Chemicals, United Kingdom. Anhydrous sodium acetate (CH_3COONa) was purchased from Chem Soln, while vanadium (IV) oxide sulfate hydrate ($VOSO_4$, 97%) was obtained from Sigma Aldrich, USA. Nitric acid (HNO_3, 69%) was obtained from Friendemann Schmidt Chemical, Germany; absolute ethanol (C_2H_6O), sulfuric acid (H_2SO_4, 95-98%) and sodium sulfate (Na_2SO_4) were purchased from Merck, Germany; FTO glass was purchased from Kaivo Optoelectronic Technology, China. All the reagents were of analytical grade and used without further purification.

2.2. Fabrication of $BiVO_4$ and $V_2O_5/BiVO_4$ photoanodes

FTO substrates were cleaned using acetone, ethanol, and deionised water in an ultrasonic bath for 20 min before being dried in the oven. $BiVO_4$ photoanode was synthesized via a facile electrodeposition synthesis method in a three-electrode PEC cell that comprised of a FTO, a Pt rod, and a Ag/AgCl (3M) electrode used as the working, counter, and reference electrodes, respectively. The electrodeposition synthesis method of monoclinic clinobisvanite $BiVO_4$ was adapted from Seabold *et* al [7]. Briefly, 35 mM $VOSO_4$ were dissolved in 0.5 M HNO_3, and 10 mM $Bi(NO_3)_3$ were then added. Thereafter, 2 M CH_3COONa solution was used to increase the pH of the mixture to pH 5.1 and stabilise the Bi(III) ions otherwise it will insoluble at pH 4.7. The final pH of the mixture was adjusted to pH 4.7 using HNO_3. The electrodeposition synthesis process was conducted potentiostatically with an applied potential of 1.9 V vs Ag/AgCl (3M) for 45 min on bare FTO and FTO/V_2O_5. After that, the as-deposited amorphous $BiVO_4$ thin film was washed using deionised water to remove the presence of any ions followed by annealing treatment at 400 ℃ for 1 hr. It was observed that the colour of the as-deposited amorphous $BiVO_4$ thin film changed from being a brownish gray film into a vivid yellow film after the annealing treatment.

2.3. Fabrication of orthorhombic V_2O_5 and $V_2O_5/BiVO_4$ photoanode

V_2O_5 thin film was obtained from a single direct anodic deposition step at 1.5 V vs Ag/AgCl (3M) from a solution of 0.2M $VOSO_4$ in 20mL of deionised water and 20mL of absolute ethanol for 10 min on bare FTO and FTO/$BiVO_4$ thin films. The final pH of the mixture was adjusted to pH 1.8 by adding H_2SO_4. Subsequently, both the thin films were annealed at 400 ℃ for 1 hr.

2.4. Characterisation

Both TEM and HR-TEM) images were obtained using a JEOL JEM-2100F electron microscope. UV–vis absorbance spectra were recorded using a spectrophotometer (Agilent, Cary 100) equipped with an integrated sphere. The absorbance spectra were analysed under ambient temperature within the wavelength range of 400 to 800 nm. The Raman spectra were recorded from a Raman spectrometer (Horiba Scientific) with a solid state laser operating at an excitation source of 514 nm. The crystal structures were characterised using an XRD (Bruker D8) by employing Cu-Kα radiation with 40 kV and 100 mA at 0.02° s^{-1} scan rate. XPS measurements were carried out by using a scanning X-ray microprobe PHI Quantera II (Ulvac-PHI, INC.) with a monochromatic Al-Kα ($h\nu$ = 1486.6 eV) X-ray source. Prior to the deconvolution of peaks, all binding energies were referenced to the adventitious carbon signal (C 1s peak) at 284.6 eV.

2.5. Electrochemical analysis

PEC measurements were carried out in a standard three-electrode assembly using an applied potentiostat/galvanostat (Metrohm PGSTAT 204 model, Netherlands), where the saturated Ag/AgCl (3M) electrode and Pt rod were used as the reference and counter electrodes, respectively. LSV scans under dark and visible light illumination were recorded. A 150 W Xenon light with an output illumination intensity of 100mW/cm^2 was used for the illumination with a scan rate of 10 mV/s. All the LSV scans, Nyquist plot and Mott-Schotty analyses were conducted in a 0.5 M aqueous Na_2SO_4 solution. The charge separation and charge injection properties of the photoanodes were investigated in the presence hydrogen peroxide (H_2O_2) as the

hole scavenger. EIS was conducted with a frequency range of 100 kHz–0.1 Hz at 1.2 V bias voltage. Mott-Schottky analyses were performed at 10 kHz by scanning the potential range from -0.1 to 0.9 V at 0.05 V s^{-1} sweep rate. IMPS measurements were conducted using a potentiostat (IVIUM technology). The electrolyte used was 0.1 M aqueous Na_2SO_4 solution. Modulated illumination (LED: cool white light) was provided by a ModuLight-module (IVIUM technology). A modulation depth of ca.10 % was used and the frequency range was 10 kHz-0.1 Hz.

3. Results and Discussion

To ensure the careful interfacial engineering between $BiVO_4$ and V_2O_5, both TEM and HR-TEM for $V_2O_5/BiVO_4$ were analyse and the images are shown in Fig. 1. The TEM image of $V_2O_5/BiVO_4$ as shown in Fig. 1 (a) evinced the existence of $BiVO_4$ and V_2O_5. To further prove the formation of heterojunction and observe inner crystal structure of $V_2O_5/BiVO_4$ photoanode, HR-TEM was employed and the corresponding images are shown in Fig. 1 (b). The HR-TEM images clearly revealed two distinct set of lattice fringes. One set of the fringe spacing measured at 0.308 nm was assigned to the (121) lattice spacing of monoclinic clinobisvanite $BiVO_4$. The second set of the fringe spacing measured at 0.207 nm was corresponded to the (010) plane of orthorhombic V_2O_5 [28, 35]. Furthermore, the HR-TEM images in Fig. 1 (c) also demonstrated the interlocked lattice fringes in the $V_2O_5/BiVO_4$ heterojunction structure instead of a simple mechanical mixture of two individual thin films. This is beneficial to the separation efficiency of photogenerated charge carriers and thus, leading to the improvement of photocurrent generation (results as shown later).

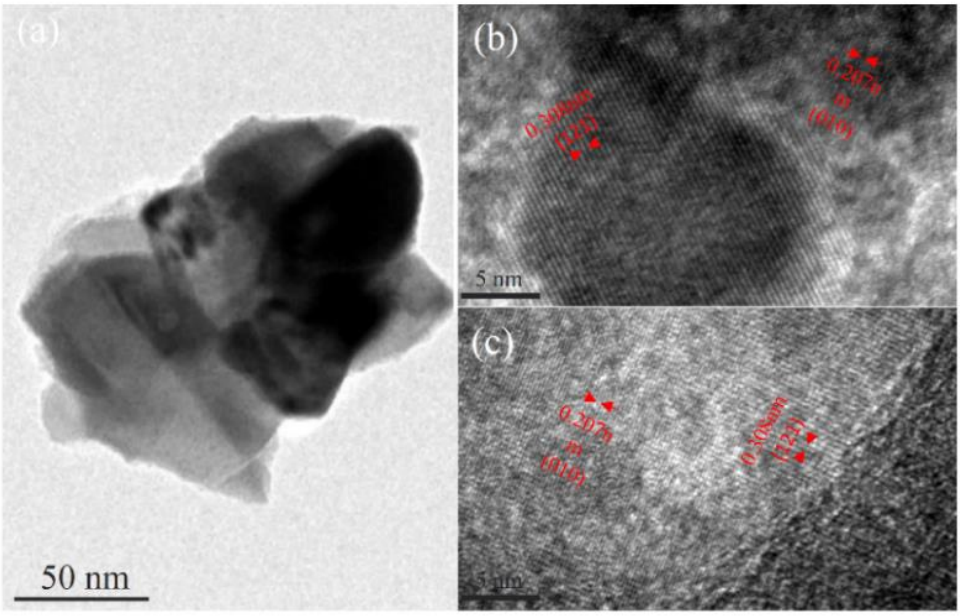

Fig. 1. (a) TEM image, (b) and (c) HR-TEM images of $V_2O_5/BiVO_4$ heterojunction photoanode.

XRD analyses were performed to verify the crystalline phases of $BiVO_4$ and V_2O_5, and the resulting XRD diffractograms are shown in Fig. 2. From the XRD spectrum of $BiVO_4$ (red line), all the diffraction peaks of 2θ= 18.5, 26.1, 28.6 and 29.5° are well indexed to the monoclinic clinobisvanite $BiVO_4$ phase that is highly photoactive because of its particular crystal and electronic structure [36, 37]. On the other hand, the pristine V_2O_5 shows XRD peaks (yellow line) that could be matched to the orthorhombic V_2O_5 phase at 20.1, 21.3 and 30.7° [38]. The XRD patterns of the composite films (green & blue lines) are nearly unchanged after forming the $V_2O_5/BiVO_4$ and $BiVO_4/V_2O_5$ heterojunction films.

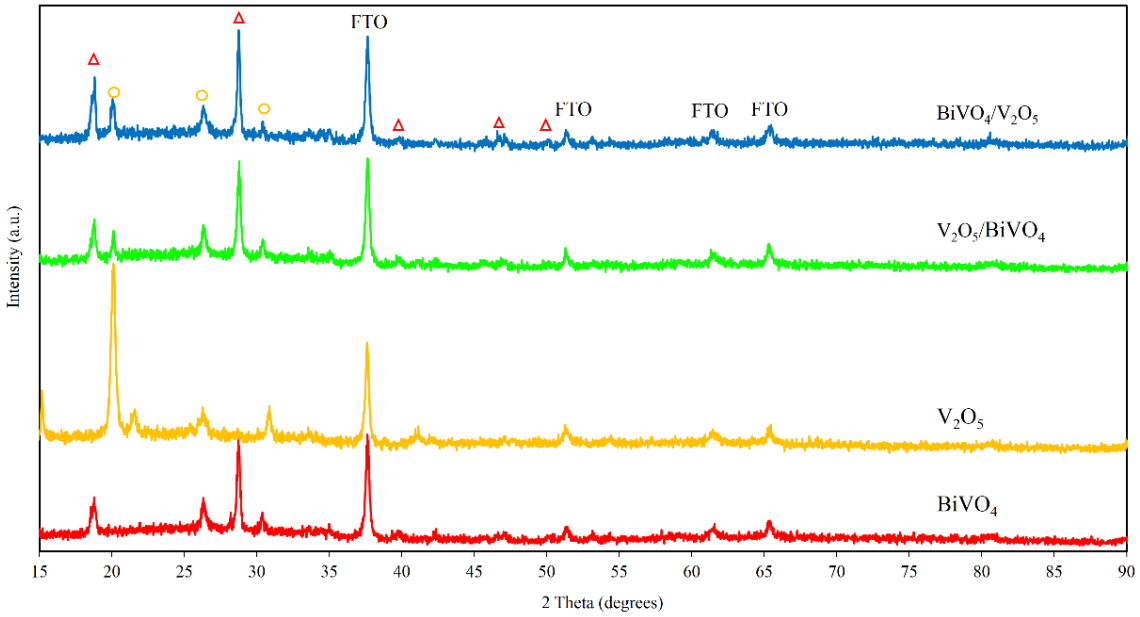

Fig. 2. XRD spectra of pristine $BiVO_4$, V_2O_5, $V_2O_5/BiVO_4$ and $BiVO_4/V_2O_5$ heterojunction photoanodes.

Raman spectra shown in Fig. 3 are in a good agreement with the XRD analyses. For the monoclinic clinobisvanite $BiVO_4$, the characteristic Raman peaks at 124, 210, 324, 363, 710 and 824 cm^{-1} can be observed. The characteristic Raman peaks of the pristine $BiVO_4$ at 124 and 210 cm^{-1} are the external mode of $BiVO_4$ that gives little structural information [39]. Whilst the characteristic Raman peaks at 324 and 363 cm^{-1} are assigned to the asymmetric and symmetric deformation modes of the VO_4^{3-} tetrahedron, respectively. Lastly, the characteristic Raman peaks at 710 and 824 cm^{-1} are attributed to the two different types of V-O stretching [40]. While for orthorhombic V_2O_5, the high wavenumber peak at 995 cm^{-1} is caused by the stretching mode of the vanadium-oxygen double bond, V=O. The second and third peak at 700 cm^{-1} and 526 cm^{-1} are assigned to the $V–O_1$ and $V–O_2$ bond, respectively. Following that, the bending motion of the $V–O_1$ and $V–O_2$ bond are corresponding to the low wavenumber peaks at 480 cm^{-1} and 302 cm^{-1}, respectively [41]. The peaks that appeared at 403 cm^{-1} and 282 cm^{-1} are assigned to the bending

motion of the shortest V=O bonds of the pristine V_2O_5 [42]. Last of all, the lower Raman shift peaks detected at 195 cm^{-1} and 147 cm^{-1} are caused by the vibrational movements of the V atoms [43]. From the Raman analyses, there is no change of band position was observed after the formation of heterojunction films. Based on the XRD and Raman analyses, it can be concluded that the monoclinic clinobisvanite $BiVO_4$ and orthorhombic V_2O_5 were successfully synthesized leading to the then formation of heterojunction films of $BiVO_4/V_2O_5$ and $V_2O_5/BiVO_4$.

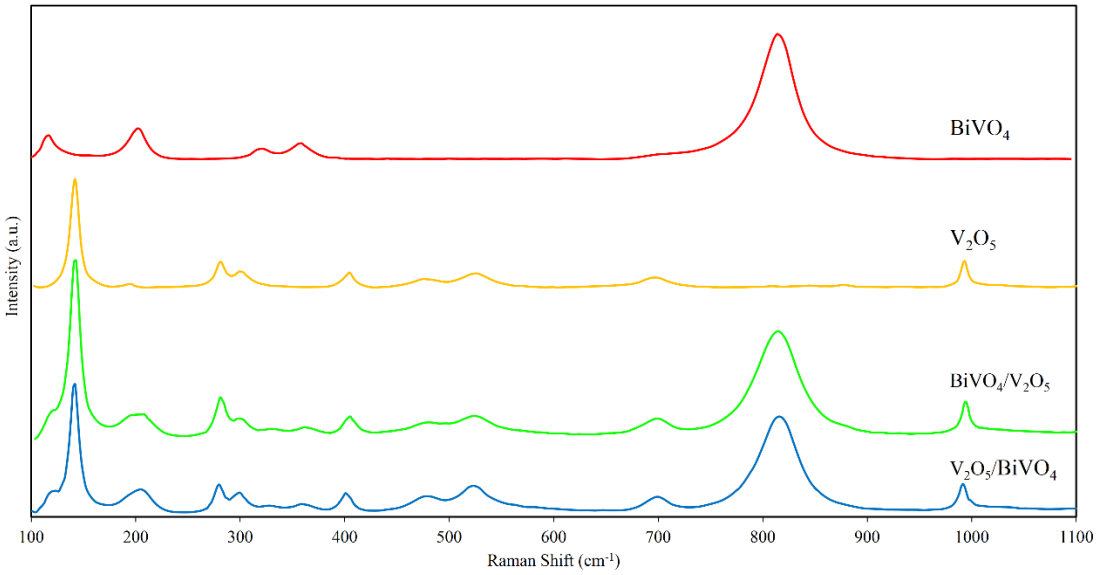

Fig.3. Raman spectra of $BiVO_4$, V_2O_5, $V_2O_5/BiVO_4$ and $BiVO_4/V_2O_5$ heterojunction photoanodes.

Additional insights into the chemical compositions of the $V_2O_5/BiVO_4$ heterojunction photoanode were further revealed through XPS analysis. Fig. 4(a) shows the overall XPS spectrum of $V_2O_5/BiVO_4$ heterojunction photoanode, revealing the presence of Bi, C, O, Sn and V elemental characteristic peaks. The observed peaks of C 1s at 284.6 eV and Sn 3d at 486.60 and 495.02 eV are attributed to the signals from carbon in instrument and FTO substrate, respectively. Whilst the peak of O 1s at 529 eV is corresponding to the O^{2-} anions.

The high resolution XPS spectrum (Fig. 4b) of Bi 4f region for $V_2O_5/BiVO_4$ heterojunction photoanode shows two main peaks with the binding energies of 158.9 and 164.2 eV, which are attributed to the Bi $4f_{5/2}$ and Bi $4f_{7/2}$, respectively. In the observed V 2p spectra shown in Fig. 4 (c), the V $2p_{2/3}$ and V $2p_{1/2}$ peaks that locate at different positions are due to the different chemical environment of the V^{5+} cations in $BiVO_4$ and V_2O_5. The V^{5+} cations in $BiVO_4$ and V_2O_5 are denoted as V_1 and V_2, respectively. V_1 gives rise to the V $2p_{2/3}$ and V $2p_{1/2}$ peaks at 517.2 and 524.2 eV, respectively while the V2 peak has binding energy at 517.7 and 525.3 eV.

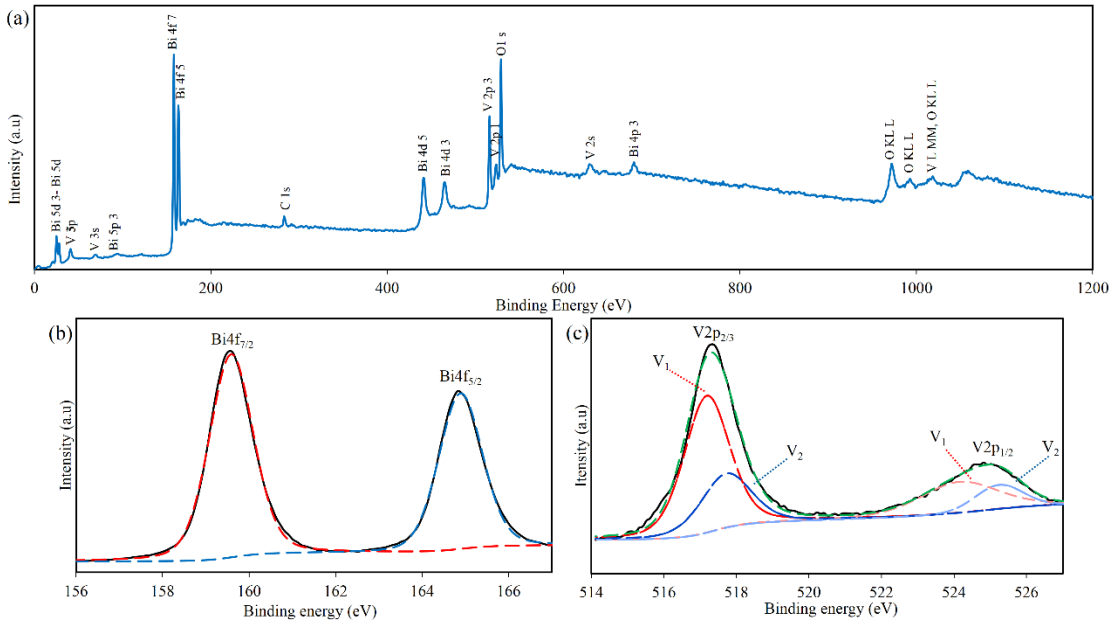

Fig.4: (a) Overall XPS spectrum of $V_2O_5/BiVO_4$ heterojunction photoanode. XPS spectra of (b) Bi 4f and (c) V 2p of $V_2O_5/BiVO_4$ heterojunction photoanode.

LSV were carried out to assess the effect of forming a heterojunction between $BiVO_4$ and V_2O_5 on the photocurrent generation potential. Fig. 5 (a) shows that the photocurrent increases with the increase in applied anodic potential under light irradiation, indicating that pristine $BiVO_4$ and V_2O_5 exhibit the *n*-type semiconductor characteristic. For the pristine $BiVO_4$ photoanode, the

onset potential under light irradiation was measured to be 0.3 V vs. Ag/AgCl. The highest photocurrent density of 0.22 mA/cm^2 at 1.5 V vs Ag/AgCl was measured for pristine $BiVO_4$. When a V_2O_5 thin film was introduced on top of $BiVO_4$, the resulting $BiVO_4/V_2O_5$ heterojunction structure yielded a photocurrent density of 0.42mA/cm^2 at 1.5 V vs Ag/AgCl that was a 2.5-fold increase in photocurrent density than the pristine $BiVO_4$. Interestingly, the photocurrent density of reverse order $V_2O_5/BiVO_4$ heterojunction photoanode was measured to be 1.53 mA/cm^2 at 1.5 V vs Ag/AgCl. In this instance, the photocurrent density of $V_2O_5/BiVO_4$ heterojunction photoanode achieved a 6.9-fold and a 7.3-fold improvement over the individual pristine $BiVO_4$ (0.22 mA/cm^2) and V_2O_5 (0.21 mA/cm^2), respectively. After forming the heterojunction structures, the photocurrent density did not reach saturation even at the applied potentials of more than 1.5 V vs Ag/AgCl where the dark current was measured relatively low at 0.02 mA/cm^2. The enhancement in photocurrent generation was attributed to the improved charge injection efficiency in the heterojunction photoanode by using H_2O_2 aqueous solution as the hole scavenger. The role of H_2O_2 is to manifest the photocurrent to be solely generated from the bulk, without the interference of surface recombination that occurs at the electrode-electrolyte interface. Therefore, the enhanced photocurrent shown in Fig. 5 (b) of $V_2O_5/BiVO_4$ when compared to pristine $BiVO_4$ is due to the promising effect of V_2O_5 in promoting effective transfer of photogenerated charge carriers. Besides, the onset potential of $V_2O_5/BiVO_4$ was cathodically shifted towards a lower potential value, indicating an augmented band bending effect in the vicinity of $BiVO_4$/electrolyte interface that facilitates the migration of holes from bulk to interface [44].

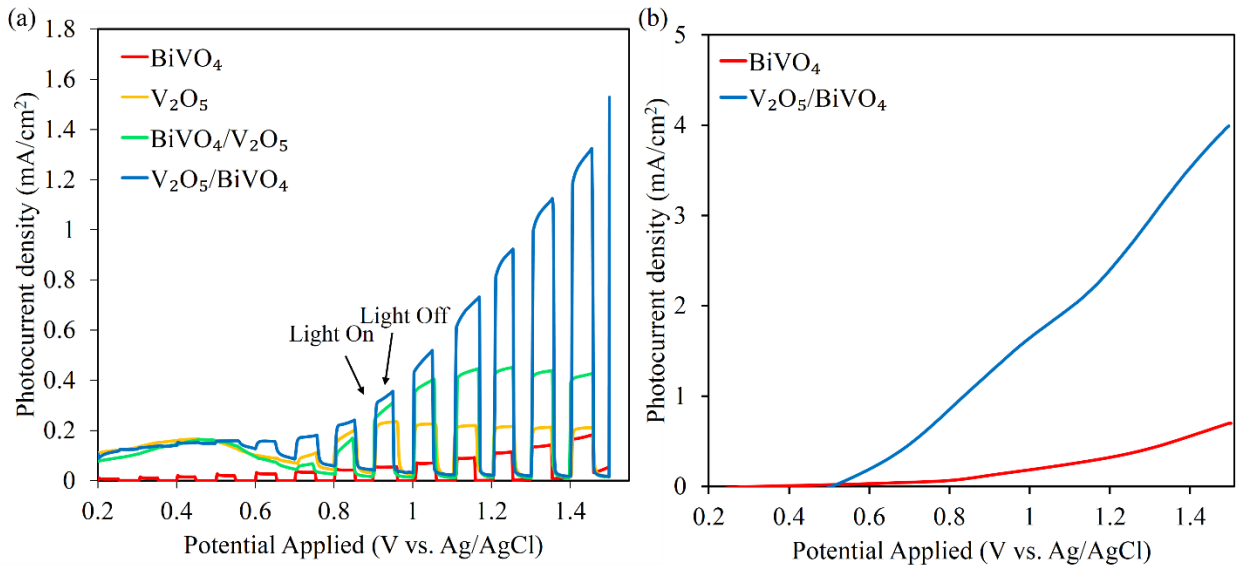

Fig. 5. (a) LSV curves of $BiVO_4$, V_2O_5, $V_2O_5/BiVO_4$ and $BiVO_4/V_2O_5$ heterojunction photoanodes under chopped light irradiation. (b) LSV curves of pristine $BiVO_4$ and $V_2O_5/BiVO_4$ photoanodes in the presence of H_2O_2 hole scavenger in 0.5 M Na_2SO_4 electrolyte.

Fig. 6 shows the chronoamperometric comparison of pristine $BiVO_4$ and V_2O_5, and heterojunction structures of $BiVO_4/V_2O_5$ and $V_2O_5/BiVO_4$ under chopped light irradiation with an irradiated surface area of 2.4 cm^2 at a constant applied potential of 1 V vs Ag/AgCl. Photocurrent decay (i.e. anodic peak) was observed for pristine $BiVO_4$ and $V_2O_5/BiVO_4$ upon initial light irradiation. The occurrence of anodic peak is associated with rapid surface recombination due to the built-up of photogenerated holes and slower charge transfer process at the photoanode-electrolyte interface. The surface recombination of photogenerated charge carriers is usually caused by either the accumulation of electrons or holes in the bulk and at the surface, respectively. However, cathodic peak can barely be observed when the light is switched off. Its presence is usually attributed to the back reaction of minority charge carriers that are trapped at the surface of conduction band. $V_2O_5/BiVO_4$ achieved 0.268 mA/cm^2, which was 22

times than the pure $BiVO_4$ (0.012 mA/cm^2), 1.4 times than pure V_2O_5 (0.185 mA/cm^2) and 1.2 times than $BiVO_4/V_2O_5$ (0.225 mA/cm^2) after under light irradiation of 5 min. This indicates that the heterojunction structure of $V_2O_5/BiVO_4$ is more photoactive, as it allows electron injection from $BiVO_4$ into V_2O_5 and overcomes the high bulk and surface recombination rate of pristine $BiVO_4$.

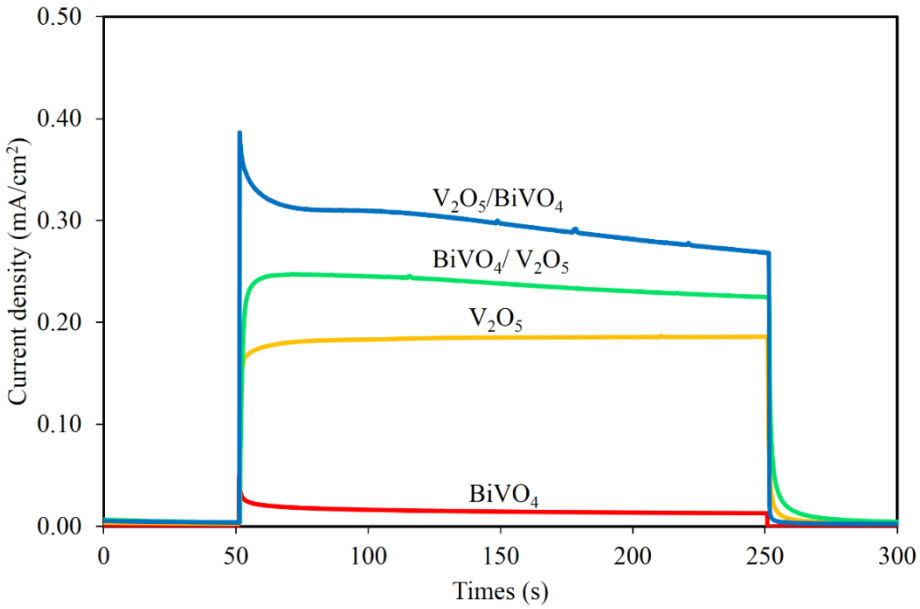

Fig. 6. Transient photocurrent response measured at an applied potential of 1V vs Ag/AgCl.

Following this, EIS Nyquist analysis was carried out to gain further insights into the photogenerated charge carriers transfer process in the heterojunction structures. Fig. 7 shows the Nyquist plot, where the real part of impedance ($Z^{'}$) is located on the z-axis (Ω) while the imaginary part of impedance ($Z^{''}$) is located on the y-axis (Ω). From Fig. 7, the spheres represent the experimental data points while the lines are the fitted simulation electrochemical impedance responses according to the equivalent circuit model used. Generally, the arc radius of the Nyquist plot provides information on the interfacial layer resistance and charge transfer properties of the

photoanode [45]. A larger diameter of arc radius implies that the charge transfer is a limiting process, and this can be ascribed to the charge transfer resistance at the photoanode-electrolyte junction. Whilst the smaller diameter of arc radius reveals the lower charge transfer resistance, which intuitively will promote a better migration of photogenerated charge carriers. Fig. 7 (inset) shows the Randles-Ershel model equivalent circuit consisting of the solution resistance (R_s), constant phase element (Q) and charge transfer resistance across the interface (R_{ct}) together with their fitted values. With the rational design of heterojunction photoanodes in this study, R_{ct} for V_2O_5/ $BiVO_4$ was significantly reduced by 2 fold. This will have a direct influence on the efficient transfer of photogenerated charge carriers at the photoanode-electrolyte interface, which could be further induced by the constructed band alignment between the semiconductors of V_2O_5 and $BiVO_4$. However, EIS analysis is not directly applicable for the photoanode-electrolyte interface due to the potential variations that appear mainly across the space charge region of the semiconductor rather than across the Helmholtz layer. Therefore, IMPS was used to analyse the direct competition between photogenerated holes transfer and surface recombination at the photoanode-electrolyte interface by modulating the light intensity.

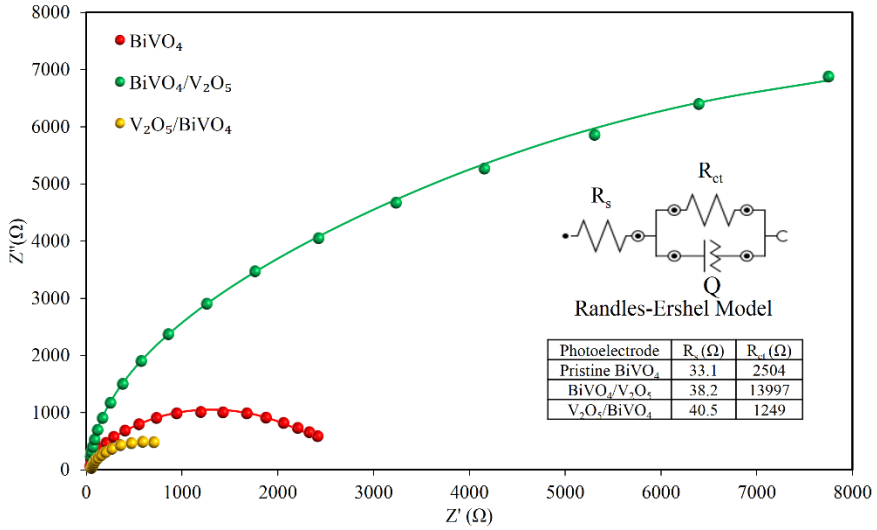

Fig. 7. Electrochemical impedance spectroscopy (EIS) Nyquist plots for $BiVO_4$-based heterojunction photoelectrode under simulated light irradiation. The upper-right inset is the equivalent electric circuit the EIS fitting values of the equivalent circuit model parameters.

In principal, the rate constants of surface recombination (K_r) and charge transfer (K_t) can be obtained by analysing the transient photocurrent responses. In practice, however, IMPS is a more robust measurement method used to characterise charge transfer and surface recombination. IMPS involves the modulation of light intensity while simultaneously measuring the magnitude and phase of the photocurrent response as a function of frequency [46]. The modulated irradiation will result in the generation minority carrier fluxes into the photoanode-electrolyte interface, which will subsequently be involved in the charge transfer reaction or combination with the majority carriers. The main advantage of IMPS is that it involves a small amplitude modulation (typically <10 % of the DC irradiation level) and hence, the changes in band bending induced by irradiation are minimised [47]. Fig. 8 (a) shows the IMPS spectra for pristine $BiVO_4$ under AM 1.5 simulated solar light irradiation. At low frequency, the semicircle located in the upper quadrant of the complex plane is known as the "recombination semicircle" because it is dominated by the surface recombination [48]. Meanwhile, the imaginary component of photocurrent reaches the maximum when the frequency (ω_{max}) matches with the characteristic relaxation constant of the system:

$$\omega_{max} = K_r + K_t$$

where K_r and K_t are the pseudo-first order charge transfer (s^{-1}) and recombination rate constants (s^{-1}), respectively. At high frequency, the response is attenuated by the total resistance in series, combined space charge and Helmholtz capacitance of the photoanode sample [48]. The radial frequency corresponding to the maximum in the semicircle is equal to $K_r + K_t$, and the ratio of

the low-to-high frequency intercept is used to estimate the charge transfer efficiency ($\frac{K_t}{K_r+K_t}$) [46]. From Fig. 8 (a), the ratio of the low-to-high frequency intercept increases as the applied bias potential is increased for pristine $BiVO_4$ photoanode. This response is expected due to the charge transfer efficiency and recombination is decreased at higher positive potential. Whilst Fig. 8 (b) shows that the K_r of pristine $BiVO_4$ photoanode is much larger than K_t and there are no significant decrement of the K_r by increasing the applied potential. Based on the complex IMPS plot for pristine $BiVO_4$ photoanode, it can be observed that the performance of pristine $BiVO_4$ photoanode is limited by the severe charge recombination on photoanode surface. Fig. 8 (c) shows that the IMPS responses of heterojunction photoanodes of $V_2O_5/BiVO_4$ and $BiVO_4/V_2O_5$, where recombination semicircles are absent at the upper quadrant. This is due to the microwave reflectivity that detects the decay of photogenerated charge carriers located at the photoanode surface, regardless of whether they are transferred across the interface or recombine with the majority carriers [49]. In this instance, the good separation efficiency of photogenerated electrons and holes in the heterojunction photoanodes leads to the vast improvement in photocurrent generation potential.

Additionally, the transit time (τ) of photogenerated charge carriers within the studied photoanode structures could also be estimated through the frequency at the apex of lower RC semicircle in the IMPS response:

$$\tau = (2\pi\mu f_{max})$$

where f_{max} is the minimum characteristic frequency of the IMPS response at the imaginary plots. Through estimation, the transit time (τ) for photo-injected electrons in the heterojunction photoanodes of $V_2O_5/BiVO_4$ and $BiVO_4/V_2O_5$ reaching the back contact are 6.4 ms and 26.5 ms,

respectively. In conclusion, the photogenerated charge carriers transfer in heterojunction structures are varying to an extent that is determined by the band alignment and the $V_2O_5/BiVO_4$ is proven favorable in terms of fast charge transport and high photocurrent generation potential.

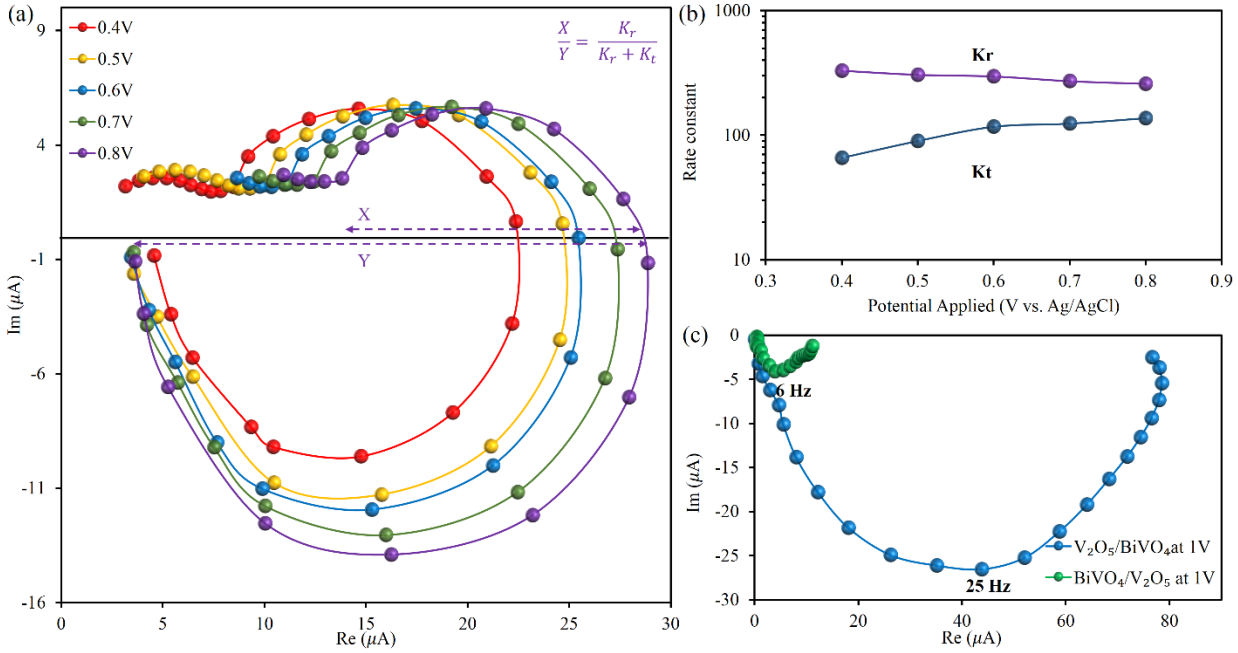

Fig. 8. (a) IMPS spectra of pristine $BiVO_4$ photoanode under different applied bias potentials under AM 1.5 simulated solar light irradiation in 0.1 M Na_2SO_4 electrolyte solution. (b) Potential dependence of the rate constants K_t and K_r for pristine $BiVO_4$ photoanode. (c) IMPS spectra of $V_2O_5/BiVO_4$ and $BiVO_4/V_2O_5$ measured at an applied potential of 1 V vs Ag/AgCl.

Finally, both the experimental Mott-Schottky analysis and Tauc plots were carried out to determine the flat-band potential (E_{fb}) and band gap energy for pristine $BiVO_4$ and V_2O_5. These will enable the reconstruction of theoretical band diagram for pristine $BiVO_4$ and V_2O_5 and heterojunction structures of $V_2O_5/BiVO_4$ and $BiVO_4/V_2O_5$ in determining their respective band alignment and heterojunction type. Furthermore, the reconstruction of theoretical band diagram also serves as an important basis used to elucidate the mechanism of photogenerated charge

carriers transfer in the much improved heterojunction structures. From Fig. 9 (a) and (b), it can be observed that the positive slopes of Mott-Schottky plots for $BiVO_4$ and V_2O_5 indicate that both of the semiconductors exhibit the *n*-type behavior. The estimated E_{fb} for pristine $BiVO_4$ and V_2O_5 were 0.35 V and 0.56 V, respectively. From Fig. 9 (c), the extrapolated straight lines are indicating that the absorption edge is due to a direct allowed transition. The intersection of the straight lines on *hv* axis corresponds to the band gap energy. The band gaps for pristine $BiVO_4$ and V_2O_5 were estimated to be approximately 2.6 eV and 2.49 eV, respectively. Working in conjugation with their E_{fb}, a theoretical band diagram for pristine $BiVO_4$ and V_2O_5 semiconductors are reconstructed from the experimental data and depicted in Fig. 9 (d). Based on the theoretical band diagram, a plausible mechanism of photogenerated charge carriers transfer in heterojunction photoanodes is schematically illustrated in Fig. 9 (e). Upon light irradiation for the heterojunction $V_2O_5/BiVO_4$ photoanode, the photogenerated electrons in CB of $BiVO_4$ migrate to the CB of V_2O_5. These electrons will eventually be transferred to the Pt counter electrode for the reduction of hydrogen ions (H^+) into molecular H_2 gas. On the other hand, the photogenerated holes at the VB of V_2O_5 migrate to the CB of $BiVO_4$ and further oxidise water molecules to produce molecular O_2 gas. As a result, the thermodynamic condition enabled the photogenerated electrons to concentrate on V_2O_5 and the holes on $BiVO_4$, efficiently facilitating the charge separation and thus enhance the PEC performance. However, for the inverse arrangement photoanode ($BiVO_4/V_2O_5$), some of the photogenerated electrons at the CB of $BiVO_4$ migrate to the substrate while some of the electrons migrate and accumulate to the CB of V_2O_5. Due to the band positions and seclusion from the electrolyte, the photogenerated holes at the VB of V_2O_5 are accumulating at the VB of $BiVO_4$ as a result of causing the recombination of the photogenerated electrons and holes at $BiVO_4$. On the basis of the above-mentioned energy

band structure, charge transfer in the Type II staggered heterojunction structures of V_2O_5/$BiVO_4$ led to a high separation efficiency of electron-hole pairs and the subsequent enhance in photocurrent generation.

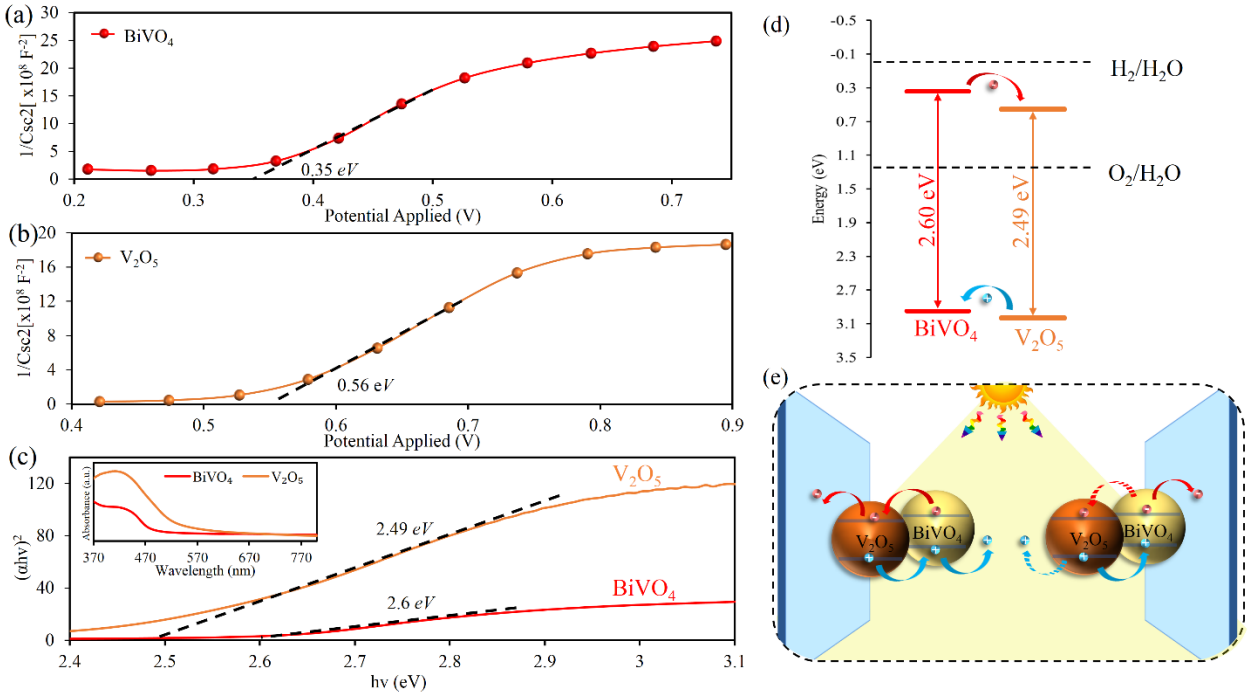

Fig. 9. Band gap characterisations of as-prepared samples: Mott-Schottky plots for pristine (a) $BiVO_4$ and (b) V_2O_5. (c) Tauc plot for the pristine $BiVO_4$ and V_2O_5 and inset displaying UV–vis diffuse reflectance spectra of $BiVO_4$ and V_2O_5. (d) Estimated relative band positions of pristine $BiVO_4$ and V_2O_5. (e) Schematic of proposed electron/hole transfer mechanism for different sequence arrangement of $BiVO_4$-based heterojunction photoelectrodes.

4. Conclusion

In conclusion, a highly efficient *n-n* Type II staggered V_2O_5/$BiVO_4$ heterojunction photoanode was successfully synthesized by studying the synergistic effect of band potentials matching and conductivity difference between pristine $BiVO_4$ and V_2O_5 thin films. Two different

heterojunction photoanode arrangements of $BiVO_4/V_2O_5$ and $V_2O_5/BiVO_4$ were systematically examined, and it was proven through Nyquist and IMPS analysis that $V_2O_5/BiVO_4$ exhibited a more effective separation of photogenerated charge carriers and rapid interfacial charge transfer. The $V_2O_5/BiVO_4$ heterojunction photoanode achieved a significantly improved photocurrent density of 1.53 mA/cm^2 at 1.5 V vs Ag/AgCl than the individual pristine $BiVO_4$ (0.22 mA/cm^2) and V_2O_5 (0.21 mA/cm^2). The improvement in the PEC performance was attributed to the wider utilisation of solar spectrum, efficient separation of photogenerated charge carriers, as well as improved charge mobility as evidenced from the much shorter transit time for the migration of photogenerated electrons to the counter electrode. As a whole, our study has demonstrated a facile electrodeposition method to fabricate a more efficient $BiVO_4$ based-heterojunction photoanode as well as chemical physics surrounding the transfer of photogenerated charge carriers within the structure. It is believed that this will pave way towards developing a highly efficient $BiVO_4$ based-heterojunction photoanode for practical application in PEC water oxidation in the near future.

Acknowledgement

Prof. MN Chong is highly indebted to the Royal Society-Newton Advanced Fellowship (Reference No.: NA150418) awarded to him in collaboration with Prof. J Tang at the University College London (UCL) Solar Energy & Advanced Materials group.

Reference

[1] T. Zhu, M. N. Chong, E. S. Chan, J.D. Ocon, Electrochemically-synthesized tungstate nanocomposites γ-WO_3/$CuWO_4$ and γ-WO_3/$NiWO_4$ thin films with improved band gap and photoactivity for solar-driven photoelectrochemical water oxidation, J. Alloys Compd. 762 (2018) 90-97.

[2] T. Zhu, M. N. Chong, E. S. Chan, J.D. Ocon, Synthesis and characterisation of a novel bilayer tungsten trioxide nanojunction with different crystal growth orientation for improved photoactivity under visible light irradiation, J. Alloys Compd. 749 (2018) 268-275.

[3] Y.W. Phuan, E. Ibrahim, M.N. Chong, T. Zhu, B.-K. Lee, O. Joey D, E. S. Chan, In situ Ni-doping during cathodic electrodeposition of hematite for excellent photoelectrochemical performance of nanostructured nickel oxide-hematite pn junction photoanode, Appl. Surf. Sci. 392 (2017) 144-152.

[4] Y.W. Phuan, W.-J. Ong, M.N. Chong, O. Joey D, Prospects of electrochemically synthesized hematite photoanodes for photoelectrochemical water splitting: A review, J. Photochem. Photobiol., C 33 (2017) 54-82.

[5] A. Fujishima, K. Honda, Electrochemical Photolysis of Water at a Semiconductor Electrode, Nature 238 (1972) 37-38.

[6] J. Su, X.-X. Zou, G.-D. Li, X. Wei, C. Yan, Y.-N. Wang, J. Zhao, L.-J. Zhou, J.0S. Chen, Macroporous V_2O_5− $BiVO_4$ composites: effect of heterojunction on the behavior of photogenerated charges, J. Phys. Chem. C 115 (2011) 8064-8071.

[7] J.A. Seabold, K.-S. Choi, Efficient and stable photo-oxidation of water by a bismuth vanadate photoanode coupled with an iron oxyhydroxide oxygen evolution catalyst, J. Am. Chem. Soc. 134 (2012) 2186-2192.

[8] J. Li, N. Wu, Semiconductor-based photocatalysts and photoelectrochemical cells for solar fuel generation: a review, Catal. Sci. Technol. 5 (2015) 1360-1384.

[9] T.W. Kim, K.-S. Choi, Nanoporous $BiVO_4$ photoanodes with dual-layer oxygen evolution catalysts for solar water splitting, Science 343 (2014) 990-994.

[10] S. Hernández, G. Gerardi, K. Bejtka, A. Fina, N. Russo, Evaluation of the charge transfer kinetics of spin-coated $BiVO_4$ thin films for sun-driven water photoelectrolysis, Appl. Catal. B 190 (2016) 66-74.

[11] S. Murcia-López, C. Fàbrega, D. Monllor-Satoca, M.D. Hernández-Alonso, G. Penelas-Pérez, A. Morata, J.R. Morante, T. Andreu, Tailoring multilayered $BiVO_4$ photoanodes by pulsed laser deposition for water splitting, ACS Appl. Mater. Interfaces. 8 (2016) 4076-4085.

[12] L. Chen, F.M. Toma, J.K. Cooper, A. Lyon, Y. Lin, I.D. Sharp, J.W. Ager, Mo-Doped $BiVO_4$ Photoanodes Synthesized by Reactive Sputtering, ChemSusChem 8 (2015) 1066-1071.

[13] J.A. Seabold, K. Zhu, N.R. Neale, Efficient solar photoelectrolysis by nanoporous Mo: $BiVO_4$ through controlled electron transport, Phys. Chem. Chem. Phys. 16 (2014) 1121-1131.

[14] K. Ding, B. Chen, Z. Fang, Y. Zhang, Z. Chen, Why the photocatalytic activity of Mo-doped $BiVO_4$ is enhanced: a comprehensive density functional study, Phys. Chem. Chem. Phys. 16 (2014) 13465-13476.

[15] H.S. Park, H.C. Lee, K.C. Leonard, G. Liu, A.J. Bard, Unbiased Photoelectrochemical Water Splitting in Z-Scheme Device Using W/Mo-Doped $BiVO_4$ and $Zn_xCd_{1-x}Se$, ChemPhysChem 14 (2013) 2277-2287.

[16] P.M. Rao, L. Cai, C. Liu, I.S. Cho, C.H. Lee, J.N. Weisse, P. Yang, X. Zheng, Simultaneously efficient light absorption and charge separation in $WO_3/BiVO_4$ core/shell nanowire photoanode for photoelectrochemical water oxidation, Nano Lett. 14 (2014) 1099-1105.

[17] J.H. Kim, J.W. Jang, H.J. Kang, G. Magesh, J.Y. Kim, J.H. Kim, J. Lee, J.S. Lee, Palladium oxide as a novel oxygen evolution catalyst on $BiVO_4$ photoanode for photoelectrochemical water splitting, J. Catal. 317 (2014) 126-134.

[18] S.K. Choi, W. Choi, H. Park, Solar water oxidation using nickel-borate coupled $BiVO_4$ photoelectrodes, Phys. Chem. Chem. Phys. 15 (2013) 6499-6507.

[19] F. Lin, D. Wang, Z. Jiang, Y. Ma, J. Li, R. Li, C. Li, Photocatalytic oxidation of thiophene on $BiVO_4$ with dual co-catalysts Pt and RuO_2 under visible light irradiation using molecular oxygen as oxidant, Energy Environ. Sci. 5 (2012) 6400-6406.

[20] X. Shi, I.Y. Choi, K. Zhang, J. Kwon, D.Y. Kim, J.K. Lee, S.H. Oh, J.K. Lim, J.H. Park, Efficient photoelectrochemical hydrogen production from bismuth vanadate-decorated tungsten trioxide helix nanostructures, Nat. Commun. 5 (2014) 4775.

[21] S.J.A. Moniz, J. Zhu, J. Tang, 1D Co-Pi modified $BiVO_4$/ZnO junction cascade for efficient photoelectrochemical water cleavage, Adv. Energy Mater.4 (2014) 1301590

[22] S. Xie, T. Zhai, Y. Zhu, W. Li, R. Qiu, Y.Tong, X. Lu, NiO decorated Mo:$BiVO_4$ photoanode with enhanced visible-light photoelectrochemical activity, Int. J. Hydrog. Energy 39 (2014) 4820-4827.

[23] X. Chang, T. Wang, P. Zhang, J. Zhang, A. Li, J. Gong, Enhanced surface reaction kinetics and charge separation of p–n heterojunction Co_3O_4/$BiVO_4$ photoanodes, J. Am. Chem. Soc. 137 (2015) 8356-8359.

[24] A.P. Singh, N. Kodan, B.R. Mehta, A. Held, L. Mayrhofer, M. Moseler, Band edge engineering in $BiVO_4$/TiO_2 heterostructure: enhanced photoelectrochemical performance through improved charge transfer, ACS Catal. 6 (2016) 5311-5318.

[25] B.-Y. Cheng, J.-S. Yang, H.-W. Cho, J.-J. Wu, Fabrication of an efficient $BiVO_4$–TiO_2 heterojunction photoanode for photoelectrochemical water oxidation, ACS Appl. Mater. Interfaces 8 (2016) 20032-20039.

[26] M.G. Lee, D.H. Kim, W. Sohn, C. W. Moon, H. Park, S. Lee, H. W. Jang, Conformally coated $BiVO_4$ nanodots on porosity-controlled WO_3 nanorods as highly efficient type II heterojunction photoanodes for water oxidation, Nano Energy 28 (2016) 250-260.

[27] Y. Pihosh, I. Turkevych, K. Mawatari, J. Uemura, Y. Kazoe, S. Kosar, K. Makita, T. Sugaya, T. Matsui, D. Fujita, Photocatalytic generation of hydrogen by core-shell WO_3/$BiVO_4$ nanorods with ultimate water splitting efficiency, Sci. Rep. 5 (2015) 11141.

[28] L. Yan, W. Zhao, Z. Liu, 1D ZnO/$BiVO_4$ heterojunction photoanodes for efficient photoelectrochemical water splitting, Dalton Trans. 45 (2016) 11346-11352.

[29] J.-S. Yang, J.-J. Wu, Low-potential driven fully-depleted $BiVO_4$/ZnO heterojunction nanodendrite array photoanodes for photoelectrochemical water splitting, Nano Energy 32 (2017) 232-240.

[30] J. Resasco, H. Zhang, N. Kornienko, N. Becknell, H. Lee, J. Guo, A.L. Briseno, P. Yang, TiO_2/$BiVO_4$ nanowire heterostructure photoanodes based on type II band alignment, ACS Cent. Sci. 2 (2016) 80-88.

[31] H. Jiang, M. Nagai, K. Kobayashi, Enhanced photocatalytic activity for degradation of methylene blue over V_2O_5/$BiVO_4$ composite, J. Alloys Compd. 479 (2009) 821-827.

[32] T.A. Khalyavka, S.V. Camyshan, N.N. Tsyba, S.N. Scherbakov, Synthesis and study of the structural, optical and photocatalytic characteristics of $V2O_5$/TiO_2 nanocomposites, J. Nano Electron. Phys. 8 (2016) 2035

[33] H. Yin, K. Yu, C. Song, R. Huang, Z. Zhu, Synthesis of Au-decorated V2O5@ ZnO heteronanostructures and enhanced plasmonic photocatalytic activity, ACS Appl. Mater. Interfaces 6 (2014) 14851-14860.

[34] Y. Hong, Y. Jiang, C. Li, W. Fan, X. Yan, M. Yan, W. Shi, In-situ synthesis of direct solid-state Z-scheme V_2O_5/gC_3N_4 heterojunctions with enhanced visible light efficiency in photocatalytic degradation of pollutants, Appl. Catal. B Environ. 180 (2016) 663-673.

[35] K. Takahashi, S.J. Limmer, Y. Wang, G. Cao, Growth and electrochemical properties of single-crystalline V_2O_5 nanorod arrays, Jpn. J. Appl. Phys. 44 (2005) 662.

[36] S. Ho-Kimura, S.J.A. Moniz, A.D. Handoko, J.Tang, Enhanced photoelectrochemical water splitting by nanostructured $BiVO_4$–TiO_2 composite electrodes, J. Mater. Chem. A 2 (2014) 3948-3953.

[37] A. Walsh, Y. Yan, M.N. Huda, M.M. Al-Jassim, S.-H. Wei, Band edge electronic structure of $BiVO_4$: elucidating the role of the Bi s and V d orbitals, Chem. Mater. 21 (2009) 547-551.

[38] V. Raju, J. Rains, C. Gates, W. Luo, X. Wang, W.F. Stickle, G.D. Stucky, X. Ji, Superior cathode of sodium-ion batteries: orthorhombic V_2O_5 nanoparticles generated in nanoporous carbon by ambient hydrolysis deposition, Nano Lett. 14 (2014) 4119-4124.

[39] J. Yu, A. Kudo, Effects of structural variation on the photocatalytic performance of hydrothermally synthesized $BiVO_4$, Adv. Funct. Mater. 16 (2006) 2163-2169.

[40] H. Yoon, M.G. Mali, J.Y. Choi, M.-W. Kim, S.K. Choi, H. Park, S.S. Al-Deyab, M.T. Swihart, A.L. Yarin, S.S. Yoon, Nanotextured pillars of electrosprayed bismuth vanadate for efficient photoelectrochemical water splitting, Langmuir 31 (2015) 3727-3737.

[41] D. Vernardou, A. Sapountzis, E. Spanakis, G. Kenanakis, E. Koudoumas, N. Katsarakis, Electrochemical activity of electrodeposited V_2O_5 coatings, J. Electrochem. Soc. 160 (2013) D6-D9.

[42] Y. Liu, X. Du, X. Liu, Effect of annealing on the properties of vanadium pentoxide films prepared by sol–gel method, Surf. Rev. and Lett. 21 (2014) 1450027.

[43] R. Baddour-Hadjean, J. Pereira-Ramos, C. Navone, M. Smirnov, Raman microspectrometry study of electrochemical lithium intercalation into sputtered crystalline V_2O_5 thin films, Chem. Mater. 20 (2008) 1916-1923.

[44] S.J. Hong, S. Lee, J.S. Jang, J.S. Lee, Heterojunction $BiVO_4/WO_3$ electrodes for enhanced photoactivity of water oxidation, Energy Environ. Sci. 4 (2011) 1781-1787.

[45] Y.W. Phuan, M.N. Chong, J.D. Ocon, E.S. Chan, A novel ternary nanostructured carbonaceous-metal-semiconductor eRGO/NiO/α-Fe_2O_3 heterojunction photoanode with enhanced charge transfer properties for photoelectrochemical water splitting, Sol. Energy Mater Sol. Cells 169 (2017) 236-244.

[46] C.Y. Cummings, F. Marken, L.M. Peter, A.A. Tahir, K.G.U. Wijayantha, Kinetics and mechanism of light-driven oxygen evolution at thin film α-Fe_2O_3 electrodes, ChemComm 48 (2012) 2027-2029.

[47] H.K. Dunn, J.M. Feckl, A. Müller, D. Fattakhova-Rohlfing, S.G. Morehead, J. Roos, L.M. Peter, C. Scheu, T.Bein, Tin doping speeds up hole transfer during light-driven water oxidation at hematite photoanodes, Phys. Chem. Chem. Phys. 16 (2014) 24610-24620.

[48] C. Zachäus F.F. Abdi, L.M. Peter, R. Van De Krol, Photocurrent of $BiVO_4$ is limited by surface recombination, not surface catalysis, Chem. Sci. 8 (2017) 3712-3719.

[49] L.M. Peter, K.G.U. Wijayantha, A.A. Tahir, Kinetics of light-driven oxygen evolution at α-Fe_2O_3 electrodes, Faraday Discuss. 155 (2012) 309-322.